RESEARCH ARTICLE

Statistical comparison of seasonal variations in the GUMICS-4 global MHD model ionosphere and measurements

L. Juusola[1], G. Facskó[1,2], I. Honkonen[1,3], P. Janhunen[1], H. Vanhamäki[1,4], K. Kauristie[1], T. V. Laitinen[1], S. E. Milan[5], M. Palmroth[1], E. I. Tanskanen[1], and A. Viljanen[1]

[1]Finnish Meteorological Institute, Helsinki, Finland, [2]Geodetic and Geophysical Institute, RCAES, HAS, Sopron, Hungary, [3]NASA Goddard Space Flight Center, Greenbelt, Maryland, USA, [4]Department of Physics, University of Oulu, Oulu, Finland, [5]Department of Physics and Astronomy, University of Leicester, Leicester, UK

Abstract Understanding the capability of a simulation to reproduce observed features is a requirement for its use in operational space weather forecasting. We compare statistically ionospheric seasonal variations in the Grand Unified Magnetosphere-Ionosphere Coupling Simulation (GUMICS-4) global magnetohydrodynamic model with measurements. The GUMICS-4 data consist of a set of runs that was fed with real solar wind measurements and cover the period of 1 year. Ionospheric convection measurements are from the Super Dual Auroral Radar Network (SuperDARN) radars, and electric currents are derived from the magnetic field measured by the CHAMP satellite. Auroral electrojet indices are used to examine the disturbance magnetic field on ground. The signatures of electrodynamic coupling between the magnetosphere and ionosphere extend to lower latitudes in GUMICS-4 than in observations, and key features of the auroral ovals—the Region 2 field-aligned currents, electrojets, Harang discontinuity, and ring of enhanced conductivity—are not properly reproduced. The ground magnetic field is even at best about 5 times weaker than measurements, which can be a problem for forecasting geomagnetically induced currents. According to the measurements, the ionospheric electrostatic potential does not change significantly from winter to summer but field-aligned currents enhance, whereas in GUMICS-4, the electrostatic potential weakens from winter to summer but field-aligned currents do not change. This could be a consequence of the missing Region 2 currents: the Region 1 current has to close with itself across the polar cap, which makes it sensitive to solar UV conductivity. Precipitation energy and conductance peak amplitudes in GUMICS-4 agree with observations.

1. Introduction

Solar irradiation, energetic particle fluxes from Sun, and the solar wind with its various structures are all potential drivers of space weather events. Therefore, understanding the chain of processes that begins with solar activity and propagates through the solar wind to Earth's magnetosphere and ionosphere is of key importance. Global self-consistent space plasma simulations, such as the magnetohydrodynamic (MHD) Grand Unified Magnetosphere-Ionosphere Coupling Simulation (GUMICS) [*Janhunen et al.*, 2012] and the recently developed hybrid-Vlasov code Vlasiator [*Sandroos et al.*, 2013; *Palmroth et al.*, 2013; *Pokhotelov et al.*, 2013; *Kempf et al.*, 2013], are an important tool for studying the solar wind-magnetosphere-ionosphere coupling. When a model is transferred from pure research purposes to operational use in space weather monitoring and forecasting, understanding its capability to reproduce different observed features in different parts of the system under different conditions becomes a key element. Thus, a central part of this process is a thorough validation of simulated features with observations. Although full of promise for the purposes of basic research, Vlasiator is yet far too heavy computationally to be used for routine space weather forecasts. A parallelized version of GUMICS (GUMICS-5) is currently under development. The much increased computing speed will allow the operation of GUMICS for forecasting space weather from upstream solar wind conditions measured at the L1 point, but some features of the MHD description may limit the range of phenomena that can be reliably modeled. Thus, thorough review of the strengths and weaknesses of GUMICS is called for in order to asses the reliability of the predictions. For example, one of the key aspects of space weather are geomagnetically induced currents (GICs) [*Boteler et al.*, 1998], which are related to temporal variations of the ground magnetic field. A current survey of the state of the art by *Pulkkinen et al.* [2013] demonstrates that neither the existing empirical models nor MHD simulations are able to reproduce the ground-based magnetic field variations sufficiently well for forecasting purposes.

GUMICS-4 consists of an MHD solar wind and magnetosphere module and an electrostatic ionosphere. Runs can be performed either by artificial solar wind input or by actual time series of measured solar wind and interplanetary parameters. Real solar wind input produces time series of dynamics, which can then be compared with observations in various parts of the magnetosphere-ionosphere system to verify the code performance and to examine the key processes during specific events. Many characteristics of the simulation are demonstrably in good agreement with observations. Recently, *Gordeev et al.* [2013] used a large set of nearly stationary GUMICS-4 solutions (162 runs altogether) with different stationary interplanetary magnetic field (IMF) and solar wind inputs generated for different dipole tilts and levels of solar EUV radiation to compare the resulting large-scale characteristics of the magnetosphere with empirical relations. They concluded that the position of the subsolar magnetopause, neutral sheet shape and position, and the plasma sheet pressure during northward IMF agrees well with statistical models. The size of the tail magnetopause, the lobe magnetic field magnitude, and the ionospheric potential, however, appeared to be systematically lower compared to empirical values.

As an MHD-based model, GUMICS-4 has some limitations. In particular, the plasma in the inner magnetosphere, which consists of overlapping hot ring current and cold plasmaspheric populations, cannot accurately be described using a single MHD fluid with a single temperature [e.g., *Janhunen et al.*, 2012]. While the motion of low-energy particles is dominated by $\mathbf{E} \times \mathbf{B}$ drift and can be modeled using MHD, the motion of the high-energy particles in the inner magnetosphere is dominated by curvature and gradient drifts not included in MHD. Some models try to represent the missing part of the physics by coupling the MHD module to some other plasma model, but GUMICS-4 does not have a separate inner magnetosphere module. Using MHD to approximate the multicomponent character of the plasma can be one reason the plasma pressure in the inner magnetosphere produced by GUMICS-4 is weak compared to observations. Possible other reasons include too coarse grid resolution and/or too large inner boundary distance (3.7 R_E). The weak pressure gradients lead to weak field-aligned current density in the ionosphere, especially the Region 2 system at the equatorward boundary of the auroral ovals. The weak Region 2 field-aligned current indicates that the rest of the auroral ovals may not be sufficiently reproduced in GUMICS-4, either, although this has not yet been comprehensively studied.

Furthermore, according to *Laitinen et al.* [2005, 2007], the entire energy flow path from the magnetopause to the ionosphere is nearly delay free in GUMICS-4, as opposed to the observed cycle of loading and subsequent unloading of magnetic energy in the tail, i.e., a substorm [*Caan et al.*, 1978]. According to *Laitinen et al.* [2005, 2007], magnetopause reconnection in GUMICS-4 is regulated by the solar wind speed and the IMF such that the location of reconnection is in accordance with the component reconnection hypothesis [*Sonnerup*, 1974; *Gonzalez and Mozer*, 1974] and tail reconnection by the energy flux through the magnetopause. Power consumption in the ionosphere, due to Joule heating and electron precipitation, directly follows the tail reconnection power. As the strongest "dB/dt events" are related to variations of auroral ionospheric currents during substorm expansion phases, it is not surprising that MHD simulations that have trouble both with substorm dynamics and the auroral oval region do not perform very well in forecasting GIC. However, there are other important aspects of space weather that the simulations can predict.

In this study, we will utilize a set of 1860 GUMICS-4 runs that was fed with real solar wind data and covers continuously the period of 1 year to perform a statistical comparison of the simulated ionosphere with observations. Because geomagnetic field lines from a large magnetospheric volume connect to the high-latitude ionospheres, observing these regions provides us with information on the entire coupled solar wind-magnetosphere-ionosphere system. Compared to the huge magnetospheric volume, the ionosphere is also a relatively small region relatively well covered with observations. Nonetheless, a statistical approach is often needed in order to accumulate enough observations to construct a global view of the ionospheric parameters. Simulations, on the other hand, are mainly run for selected events. Thus, suitable data sets for extensive measurement-model comparisons are hard to find. The recently completed set of runs provides unique possibilities for such studies. We will start by introducing the GUMICS-4 model and the measurements used (section 2) then proceed with the comparison (section 3), discuss the results (section 4), and, finally, summarize the conclusions (section 5).

2. Data

2.1. GUMICS-4 Ionosphere

GUMICS-4 consists of an MHD solar wind and magnetosphere and an electrostatic ionosphere [*Janhunen et al.*, 2012]. The MHD domain extends from $-224\,R_E < x_{GSE} < 32\,R_E$, $|y_{GSE}| < 64\,R_E$, and $|z_{GSE}| < 64\,R_E$ (Earth radii, $1\,R_E = 6371.2$ km; GSE refers to the geocentric solar ecliptic coordinate system). Solar wind temperature, density, velocity, and magnetic field are given as boundary conditions for the sunward side of the box, while for the other five sides, outflow boundary conditions are applied. The inner boundary of the MHD domain is a spherical surface at $3.7\,R_E$.

The electrostatic ionosphere is modeled as a spherical surface at 110 km altitude (the solution is not sensitive to the exact value). Electron precipitation and field-aligned currents are fed to the ionosphere by mapping them from the inner boundary of the MHD domain along a dipole magnetic field. The $3.7\,R_E$ shell maps to latitudes poleward of about $\pm 59°$ in the ionosphere, confining the ionosphere-magnetosphere coupling to these regions. Electron precipitation particle flux is computed as the thermal electron flux from the MHD plasma at the $3.7\,R_E$ shell by assuming a Maxwellian source distribution and an ion to electron temperature ratio of 4. Before using the MHD density in the electron precipitation computation, it is multiplied by the loss cone filling rate, a function which is unity inside the polar cap and goes smoothly to almost zero when the magnetic latitude decreases from 70° to 60°. The ionosphere-magnetosphere potential difference (parallel to the magnetic field) is zero by default. The resolution of the ionospheric grid is highest in the auroral ovals, about 180 km, and 360 km in the polar caps. Both the electron precipitation and UV radiation contribute to the height-integrated ionospheric Hall and Pedersen conductivities, i.e., conductances. The solar UV contribution to the conductances is obtained from the empirical formulas of *Moen and Brekke* [1993]. The background ionization due to stellar UV and cosmic rays is modeled by adding a constant term of 0.5 mho to the solar UV contributions. The electron precipitation contribution to the conductances is obtained by height integration of the conductivities, solved at a 3-D grid from the ionospheric electron density due to precipitation and the electron-neutral and ion-neutral collision frequencies as given by the Mass Spectrometer and Incoherent Scatter (MSIS) model [*Hedin*, 1991]. The ionospheric electrostatic potential (perpendicular to the magnetic field) is then solved from the conductances and field-aligned current and mapped back to the inner boundary of the MHD domain along the dipole field. More details on GUMICS can be found in *Janhunen et al.* [2012, and references therein].

In this study, we have used a set of 1860 GUMICS-4 runs that was fed with real solar wind data (1 min resolution, extracted from NASA/Goddard Space Flight Center's OMNI data set through the OMNIWeb interface http://omniweb.gsfc.nasa.gov/) and covers continuously the period from 30 January 2002 00:04:00 UT to 2 February 2003 15:49:00 UT. Any gaps in the solar wind data were filled using linear interpolation. Each run was about 4.75 h long and was preceded by a 1 h long initialization period. Each initialization was run using constant solar wind, with values corresponding to the conditions at the beginning of the respective run. The dipole tilt angle and IMF B_x component were kept constant for each run (dynamic tilt has not been implemented in GUMICS-4 and varying B_x would lead to $\nabla \cdot \mathbf{B} \neq 0$ in the solver [*Roe*, 1981; *Janhunen et al.*, 2012]), and their values were the averages of the run period. Adaptation level 5 of the adaptive MHD domain grid was used, corresponding to a minimum grid cell size of $0.25\,R_E$. The simulation output includes ionospheric distributions of the Hall and Pedersen conductances, precipitation energy flux, horizontal and field-aligned current density, electrostatic potential, and the corresponding electric field as a function of dipole latitude and magnetic local time (MLT), saved every 5 min. A more detailed description of the set of runs is in preparation (G. Facsó et al., Comparison of one year long GUMICS-4 global MHD simulation to spacecraft and ground based measurements, in preparation to submit to *Journal of Geophysical Research*, 2014).

For a straightforward time series comparison with observations, the cross polar cap potential (CPCP) for each saved epoch was computed as a difference between the maximum and minimum of the electrostatic potential distribution in the Northern Hemisphere. The 2-D spherical elementary current system (SECS) method [*Amm*, 1997; *Amm and Viljanen*, 1999] was used to divide the horizontal current density into its curl-free and divergence-free components and to calculate the auroral electrojet indices (*AL* and *AU*) corresponding to the divergence-free component. The *AL* (*AU*) index is defined as the minimum (maximum) of the north-south component of the disturbance magnetic field on ground (B_x) measured by 10 to 13 standard magnetic observatories located between 60.4° and 71.2° corrected geomagnetic latitude [*Davis and Sugiura*, 1966]. The GUMICS-4 *AL* and *AU* indices were derived as the minimum and maximum of the ground

B_x as given by the simulation at the locations of the 13 standard Kyoto stations at each moment of time. All 13 stations were assumed to provide data at all times.

2.2. Observational Ionosphere

We have used magnetic field measurements from the low-orbit Challenging Minisatellite Payload (CHAMP, http://op.gfz-potsdam.de/champ/) satellite to determine global statistical maps of the horizontal and field-aligned ionospheric electric currents at 100 km altitude as a function of Altitude Adjusted Corrected Geomagnetic Coordinates (AACGM) latitude [*Baker and Wing*, 1989] and MLT. All maps were projected onto a 40 × 40 Cartesian grid of cells 222 km × 222 km in size (222 km is equivalent to 2° of latitude), centered on the geomagnetic pole with rows and columns aligned along the noon-midnight and dawn-dusk meridians [*Milan et al.*, 2010].

The CHAMP satellite measured Earth's magnetic field from 15 July 2000 to 19 September 2010. The satellite had an almost circular, near-polar orbit with an initial altitude of 454 km and orbital period of 1.5 h. All local time sectors were covered in 131 days. We have used the 1 s vector magnetic field data (B_x: positive north, B_y: positive east, and B_z: positive down). The Potsdam Magnetic Model of the Earth (POMME) magnetic field model [*Maus et al.*, 2006] was used to subtract the baseline (POMME-4 was used for 2000–2001 and POMME-6 for 2002–2010). In order to accumulate enough measurements for reliable statistics, the entire mission period was used. The mean and the standard deviation (SD) of B_x, B_y, and B_z were calculated in each grid cell, and the 2-D SECS method was used to determine the corresponding ionospheric and field-aligned current distributions and their uncertainties.

The Super Dual Auroral Radar Network (SuperDARN) assimilates Doppler shift measurements of HF radio waves backscattered from the F region ionosphere to determine the **E** × **B** flow patterns in the northern and southern polar regions (poleward of approximately 50° latitude) [*Greenwald et al.*, 1995; *Chisham et al.*, 2007]. The electric field can be represented as an electrostatic potential pattern. Where radar measurements are insufficient to determine the electrostatic potential, they are supplemented by additional points taken from an empirical model of the convection pattern parametrized by the IMF orientation and strength [*Ruohoniemi and Baker*, 1998]. We have used a SuperDARN data set (European Cluster Assimilation Technology (ECLAT), http://cosmos.esa.int/web/csa), which comprises the electrostatic potential patterns at a cadence of 120 s from 2000 to 2010, projected onto the grid described above. To avoid parts of the potential constrained only by the statistical model, we have only utilized cells with actual observations in them (except for the calculation of CPCP). Furthermore, we have only included maps that can be considered reliable, that is, maps that contain at least 200 vectors and have a steady lower latitude boundary (known as the Heppner-Maynard boundary). The CHAMP data-based current density models and SuperDARN data-based convection models are described in more detail by *Juusola et al.* [2014].

The *AL* and *AU* indices at 1 min resolution were obtained from the World Data Center for Geomagnetism, Kyoto (http://wdc.kugi.kyoto-u.ac.jp/index.html). Because the indices are only available for the Northern Hemisphere and because the SuperDARN data coverage for the included period was much better for the Northern than for the Southern Hemisphere, we have only considered the Northern Hemisphere in this study.

3. Results

3.1. Convection

Figures 1a and 1b show 1 day median values of the Northern Hemisphere cross polar cap potential (CPCP) as a function of universal time (UT) from 30 January 2002 to 2 February 2003. For the median to be deemed acceptable, at least 10% of the day's data were required to exist. The four vertical lines in each panel denote the Northern Hemisphere spring equinox, summer solstice, fall equinox, and winter solstice, respectively. The different colors indicate the seasons (for the purpose of the statistical analysis, Figure 2): blue for winter, green for equinox, and red for summer. Figure 1a displays CPCP as simulated with GUMICS-4 and Figure 1b as measured by SuperDARN. Unlike the CPCP measured by SuperDARN, the CPCP simulated with GUMICS-4 shows a clear seasonal variation with values that are somewhat higher than those measured by SuperDARN during local winter, comparable during equinox, and clearly smaller during summer. A scatterplot of the GUMICS-4 and SuperDARN CPCP values is shown in Figure 1c. The black line is the line of equality. Although the simulated and measured CPCP values can occasionally be very close to each other during equinox and
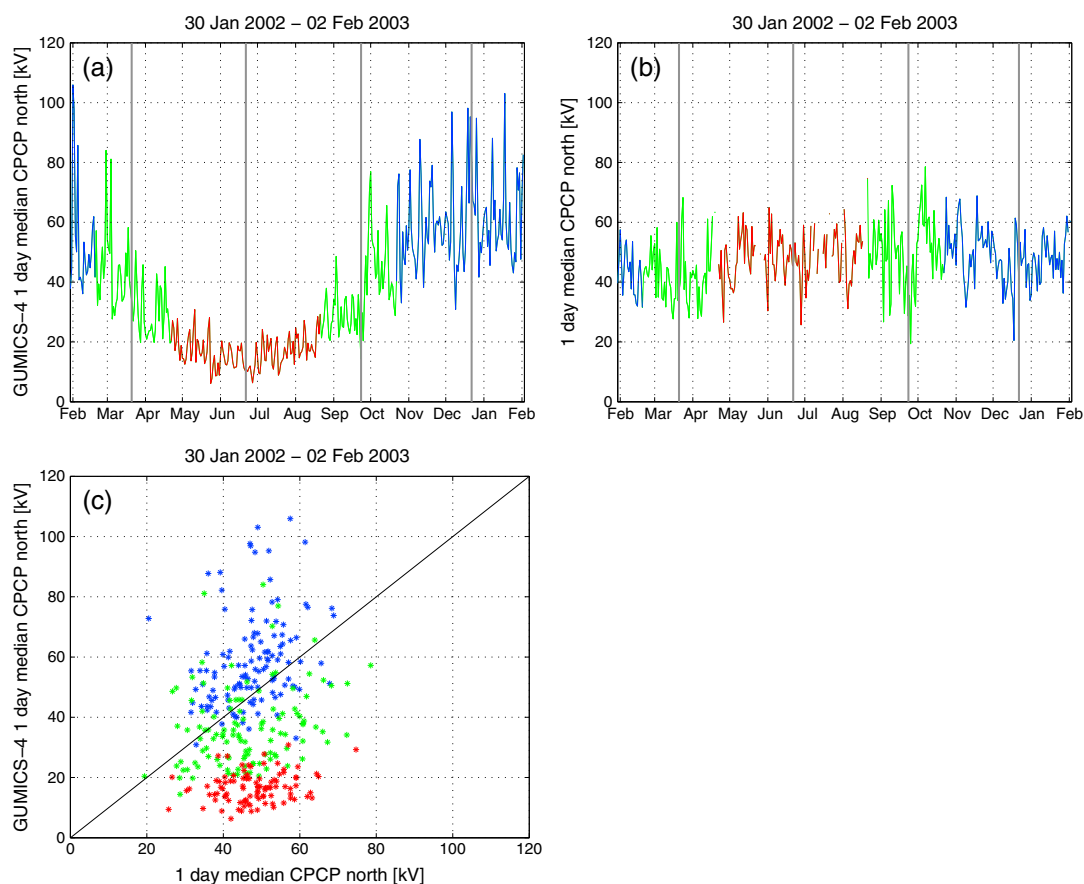
Figure 1. One day median values of the Northern Hemisphere cross polar cap potential (CPCP) as a function of UT from 30 January 2002 to 2 February 2003. The four vertical lines in each panel denote the Northern Hemisphere spring equinox, summer solstice, fall equinox, and winter solstice, respectively. The different colors indicate the seasons: blue–winter, green–equinox, red–summer. (a): CPCP from GUMICS-4 and (b): CPCP from SuperDARN. (c): GUMICS-4 CPCP as a function of SuperDARN CPCP. The line of equality is shown in black.

winter conditions, in general, the correlation is not good: the correlation coefficient for winter is 0.28, for equinox 0.26, and for summer 0.23.

Figure 2 shows the distribution of the electrostatic potential Φ (color) and the corresponding $\mathbf{E} \times \mathbf{B}$ drift (arrows) as a function of latitude and MLT. Figures 2a–2c show mean winter, equinox, and summer distributions from GUMICS-4 and Figures 2d–2f from SuperDARN. The seasons are defined as shown in Figure 1. The blue and red curves are the ± 5 kV contours of the electrostatic potential. The locations of the minimum and maximum of the mean electrostatic potential are indicated by the magenta and cyan asterisks, respectively, and the difference between the maximum and minimum value (CPCP) is given in the bottom right corner. The uncertainty of CPCP is estimated from the standard deviation (SD) of the electrostatic potential ($\Delta\Phi$, shown in Figure 3 and discussed later in this section) as $\Delta\mathrm{CPCP} = (|\min(\Phi - \Delta\Phi) - \min(\Phi)| + |\max(\Phi + \Delta\Phi) - \max(\Phi)|)/2$, where min and max refer to the spatial minimum and maximum of the distribution. The SD does not represent the measurement error but the natural variation of the potential in each grid cell.

The CPCP for the mean winter, equinox, and summer distributions are 52.0 ± 15.5 kV, 30.4 ± 11.0 kV, and 14.7 ± 5.2 kV for GUMICS-4 and 28.4 ± 9.2 kV, 30.3 ± 9.9 kV, and 36.2 ± 10.2 kV for SuperDARN. In agreement with Figure 1, the SuperDARN values remain almost constant from winter to equinox to summer, whereas the GUMICS-4 values decrease substantially. The equinox CPCP from GUMICS-4 agrees best with the CPCP from SuperDARN. In agreement with Figure 1, ΔCPCP for GUMICS-4 is substantially larger during winter than during summer, while for SuperDARN it remains almost constant throughout the seasons.

Although both GUMICS-4 and SuperDARN distributions show the expected two-cell convection pattern, the pattern from SuperDARN is confined to higher latitudes than the one from GUMICS-4. In order to check
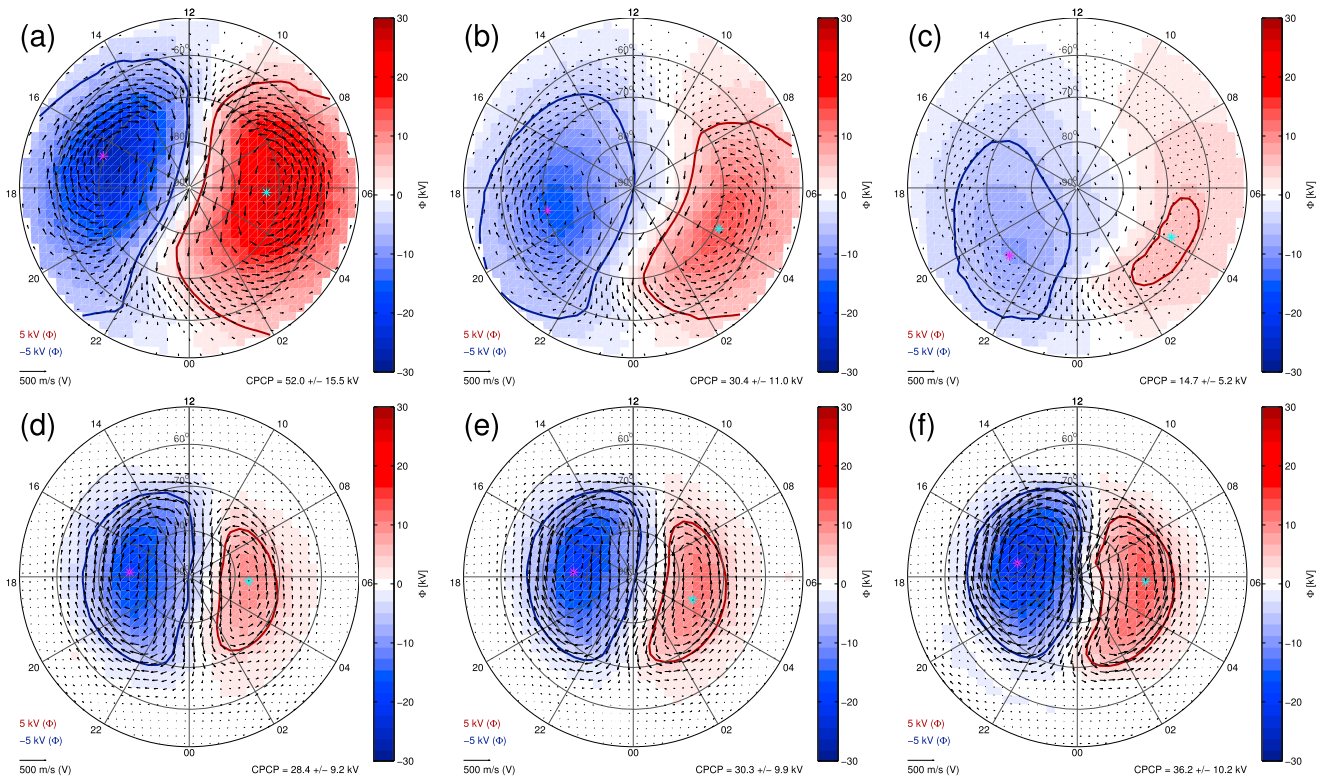
Figure 2. E × B drift (arrows) and electrostatic potential (color) for winter, equinox, and summer (a–c) from GUMICS-4 and (d–f) from SuperDARN. The blue and red curves are the ±5 kV contours of the electrostatic potential. The locations of the minimum and maximum of the potential are indicated by the magenta and cyan asterisks, respectively, and the difference between the maximum and minimum value (CPCP) is given in the bottom right corner.
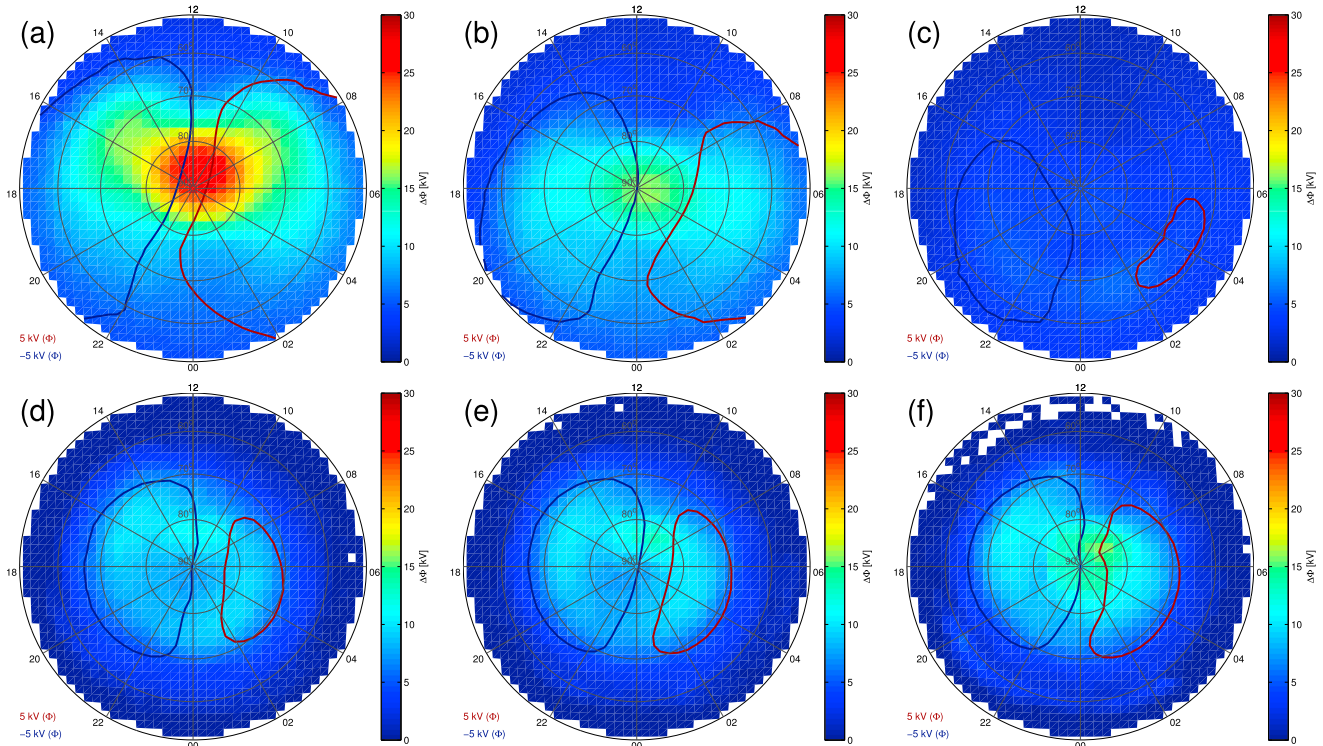

Figure 3. Standard deviation (SD) of the electrostatic potential for winter, equinox, and summer (a–c) from GUMICS-4 and (d–f) from SuperDARN. The blue and red curves are the same as in Figure 2.
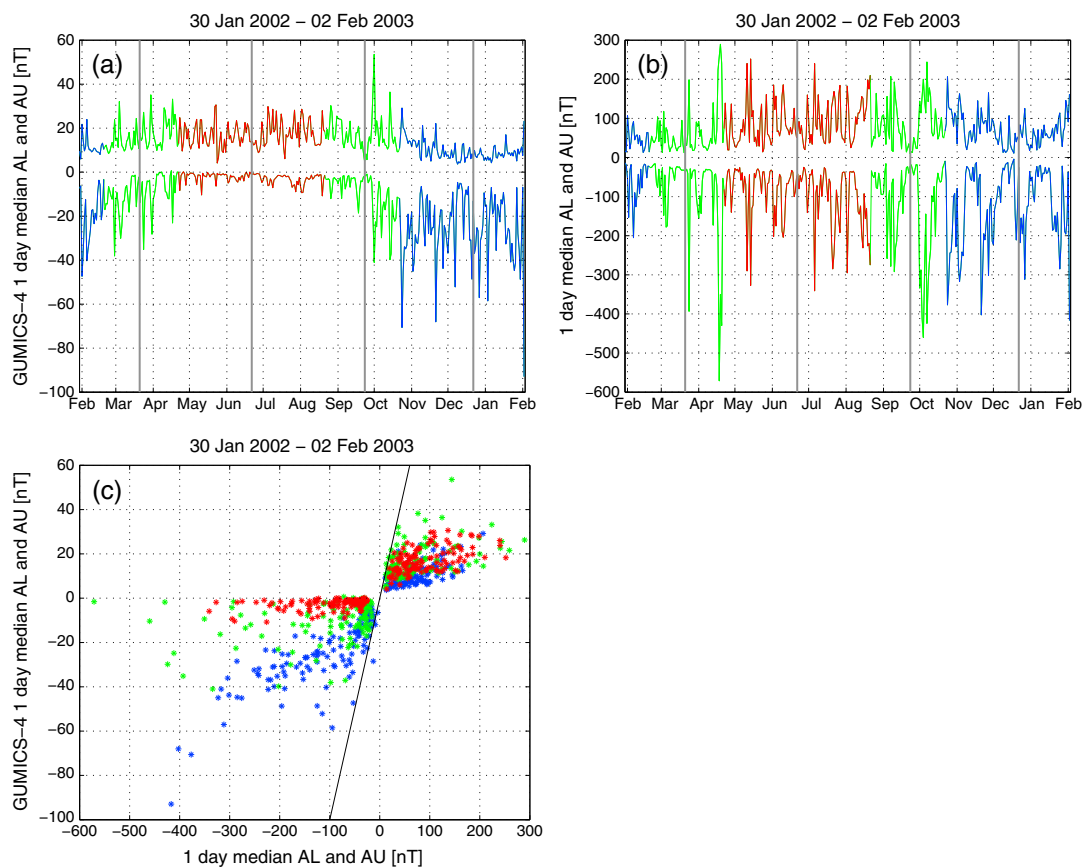
Figure 4. The same as Figure 1 except for the *AL* (negative values) and *AU* (positive values) indices instead of CPCP. (a): *AL* and *AU* from GUMICS-4. (b): Kyoto *AL* and *AU*. Note that the vertical axes for the two panels are not identical. (c): GUMICS-4 *AL* (*AU*) as a function of Kyoto *AL* (*AU*).

that this was not caused by the different time intervals used to construct the GUMICS-4 (~2002) and Super-DARN (2000–2010) distributions, we derived the patterns in Figures 2d–2f using data only from 2002 (not shown). Although the resulting patterns were more noisy due to the smaller amount of data, there were no significant differences to Figures 2d–2f. The lower latitude extent of the SuperDARN convection pattern can also be limited by the geographical locations of the radars [e.g., *Imber et al.*, 2013]. However, the convection should not extend to lower latitudes than the ionospheric current system observed by CHAMP, which is in reasonable agreement with the SuperDARN observations (sections 3.2 and 3.3). In winter, the MLT locations of the minimum and maximum potential for GUMICS-4 are more or less in agreement with the SuperDARN observations. However, toward summer the locations as given by GUMICS-4 drift toward the nightside while those given by SuperDARN remain almost stationary.

Figure 3 displays the SD of the electrostatic potential for winter, equinox, and summer from GUMICS-4 (a–c) and from SuperDARN (d–f). For reference, the blue and red curves indicate the ±5 kV contours of the mean electrostatic potential from Figure 2. For both GUMICS-4 and SuperDARN, the highest SD values can be found on the dayside at high latitudes between the convection cells. Based on the location, they are likely to be related to combining convection patterns from periods with different IMF directions [e.g., *Juusola et al.*, 2014]. Similar to the behavior of the ΔCPCP values given in Figure 2, the SD for GUMICS-4 is substantial higher during winter than during summer, while the SD for SuperDARN does not vary much, being only slightly higher during summer than during winter.

3.2. Ground Magnetic Field
Figure 4 displays the *AL* (negative values) and *AU* (positive values) indices in the same format as Figure 1. Note that the vertical axes for the two panels are not identical, as the amplitudes produced by GUMICS-4 tend to be much smaller than the measured ones. Both the simulated and measured *AU* indices display
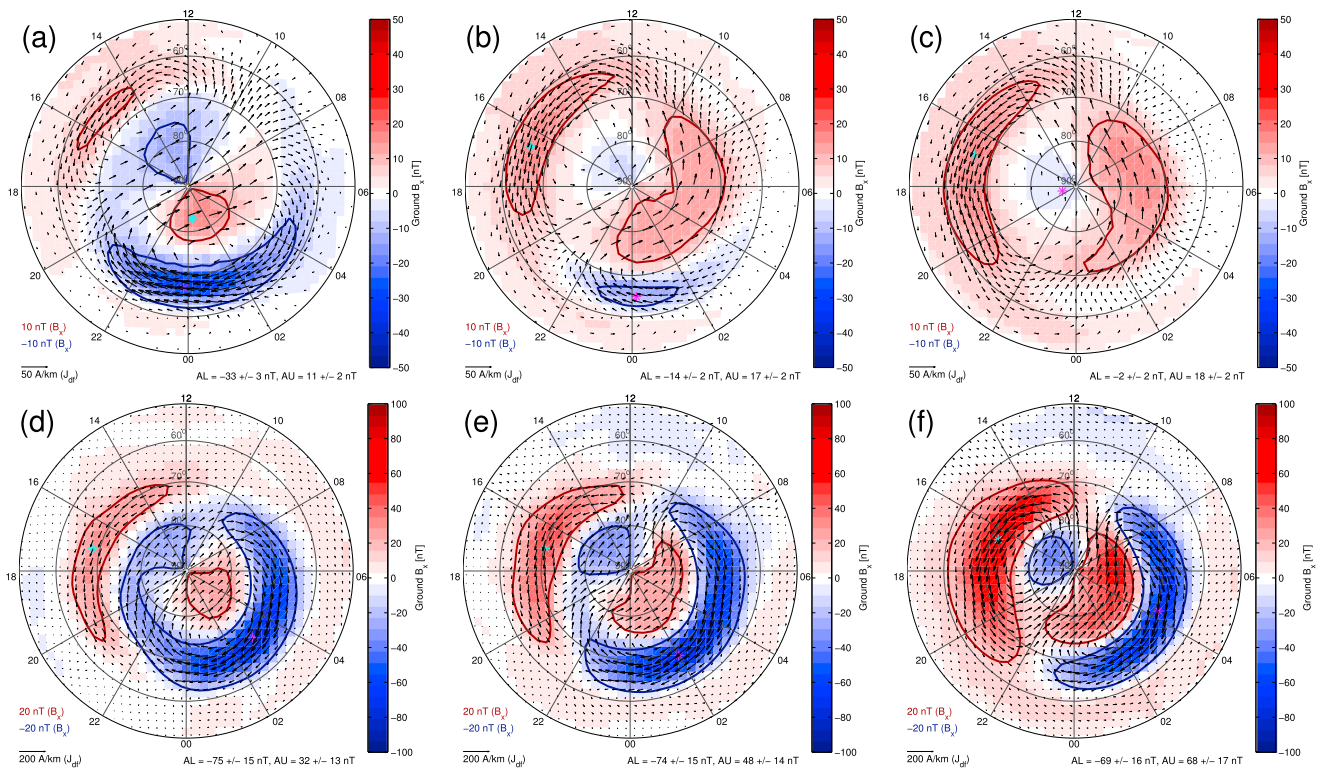
Figure 5. Divergence-free component of the horizontal current density (arrows) and ground B_x (color) for winter, equinox, and summer (a–c) from GUMICS-4 and (d–f) from CHAMP. The blue and red curves are the ±10 nT in Figures 5a–5c or ±20 nT in Figures 5d–5f contours of B_x. The locations of the minimum and maximum of B_x are indicated by the magenta and cyan asterisks, respectively. Note that the scales for the GUMICS-4 and CHAMP distributions are not identical.

a similar seasonal trend with generally weaker values during winter than summer and the largest peaks occurring during equinoxes. As expected, the largest peaks in the measured *AL* also occurred during equinoxes [*Russell and McPherron*, 1973]. GUMICS-4, however, produces the strongest *AL* peaks during winter, and toward summer the values weaken substantially. Despite the weaker amplitude of the simulated *AL*, there is a quite good correlation with the measured *AL* during winter conditions (correlation coefficient 0.80), although not during equinox (0.34) or summer (0.41). The *AU* correlation coefficients vary less with season, being 0.59 for winter, 0.46 for equinox, and 0.53 for summer. A linear fit to the winter *AL* data indicates that the GUMICS-4 *AL* is about 5 times weaker than Kyoto *AL* during winter. Because of the weak ground magnetic field amplitude, also d*B*/d*t* and, thus, GIC predicted by GUMICS-4 tend to be systematically too weak. Timing of the events tends to fail at the resolution of hours (1 h median *AL* correlation coefficient for winter is 0.55, and Kyoto *AL* linearly interpolated to the 5 min resolution of the GUMICS-4 epochs gives a correlation coefficient of 0.50 for winter), which could be related to the lack of the loading-unloading cycle in GUMICS-4 [*Laitinen et al.*, 2005, 2007].

The arrows in Figure 5 depict the divergence-free component of the horizontal ionospheric current density. As this component produces the same magnetic field below the ionosphere as the full horizontal and field-aligned current distribution [*Fukushima*, 1976; *Untiedt and Baumjohann*, 1993], it is also called the equivalent current density. The color background shows the resulting *x* component of the disturbance magnetic field (B_x) on ground. The locations of the minimum and maximum of the B_x distributions in Figure 5 are indicated by the magenta and cyan asterisks, respectively. The blue and red curves are the ±10 nT (a–c) or ±20 nT (d–f) contours of B_x. Figures 5a–5c show mean winter, equinox, and summer distributions from GUMICS-4 and Figures 5d–5f from CHAMP. The seasons are defined as shown in Figure 1 or Figure 4. Note that the scales for the GUMICS-4 and CHAMP data are not identical. The *AL* and *AU* indices corresponding to the distributions, estimated here as the minimum and maximum of B_x between 60.4° and 71.2° latitude (the *AL* and *AU* in Figure 4 were calculated taking into account the actual locations of the stations at each moment of time), are given in the bottom right corner. The uncertainties of the indices are estimated from the uncertainty of the ground B_x (ΔB_x, shown in Figure 6) as $\Delta AL = |\min(B_x - \Delta B_x) - \min(B_x)|$ and
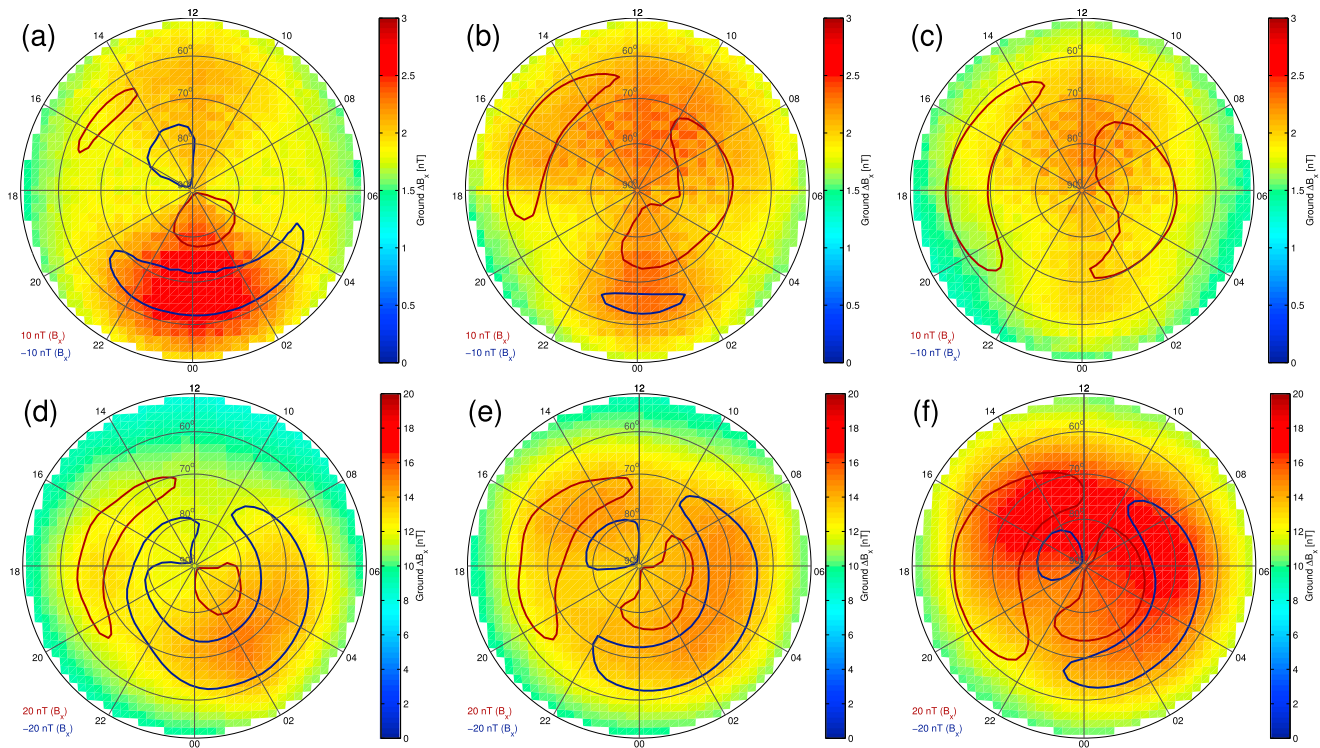
Figure 6. Uncertainty of ground B_x for winter, equinox, and summer (a–c) from GUMICS-4 and (d–f) from CHAMP. For GUMICS-4, the uncertainty is estimated from the standard deviation (SD) of the horizontal ionospheric current density (ΔJ_x and ΔJ_y) using the propagation of error and for CHAMP from the SD of the measured magnetic field (ΔB_x, ΔB_y, and ΔB_z). The blue and red curves are the same as in Figure 5. Note that the scales for the GUMICS-4 and CHAMP distributions are not identical.

$\Delta AU = |\max(B_x + \Delta B_x) - \max(B_x)|$. Again, min and max refer to the spatial minimum and maximum of the distribution.

The equivalent current pattern derived from the CHAMP measurements comprises the westward electrojet in the dawn and midnight sector auroral oval and the eastward electrojet in the dusk sector. The Harang reversal or discontinuity [e.g., *Koskinen and Pulkkinen*, 1995], i.e., the region in the premidnight sector where the two electrojets overlap such that the westward electrojet is located poleward of the eastward electrojet, is most prominent during winter (Figure 5d) and practically disappears during summer (Figure 5f). On the ground, negative B_x is observed under the westward electrojet and positive B_x under the eastward electrojet. During all seasons, the strongest negative B_x originates from the westward electrojet on the dawnside auroral oval and the strongest positive B_x from the eastward electrojet on the duskside auroral oval. The eastward electrojet enhances from winter to equinox to summer, which is reflected in the behavior of the *AU* index given in the bottom right corner of each panel. This also explains the behavior of the *AU* index in Figure 4b.

The winter pattern derived from GUMICS-4 resembles that derived from CHAMP measurements with an eastward and a westward electrojet and sunward and dawnward equivalent current in the polar cap. However, as already noted above, the GUMICS-4 polar cap extends to lower latitudes than the one derived from observations. Consequently, the poleward boundary of the electrojets is also located at lower latitudes in GUMICS-4. The equatorward boundary of the GUMICS-4 magnetosphere-ionosphere coupling is fixed at 59°, mapping to 3.7 R_E, but the electrojets do not seem to naturally fit within this latitude range. Thus, the Harang discontinuity in the premidnight sector is much less distinct in GUMICS-4 than in the CHAMP pattern. The strongest negative B_x in GUMICS-4 originates from the midnight sector of the auroral oval and the strongest positive B_x from the polar cap instead of the dawn and dusk sector ovals, respectively. From winter to equinox to summer both the eastward electrojet and the eastward equivalent current in the polar cap enhance in GUMICS-4, resulting in the disappearance of the Harang discontinuity, in agreement with CHAMP measurements. However, CHAMP does not observe any significant weakening of the dawnside
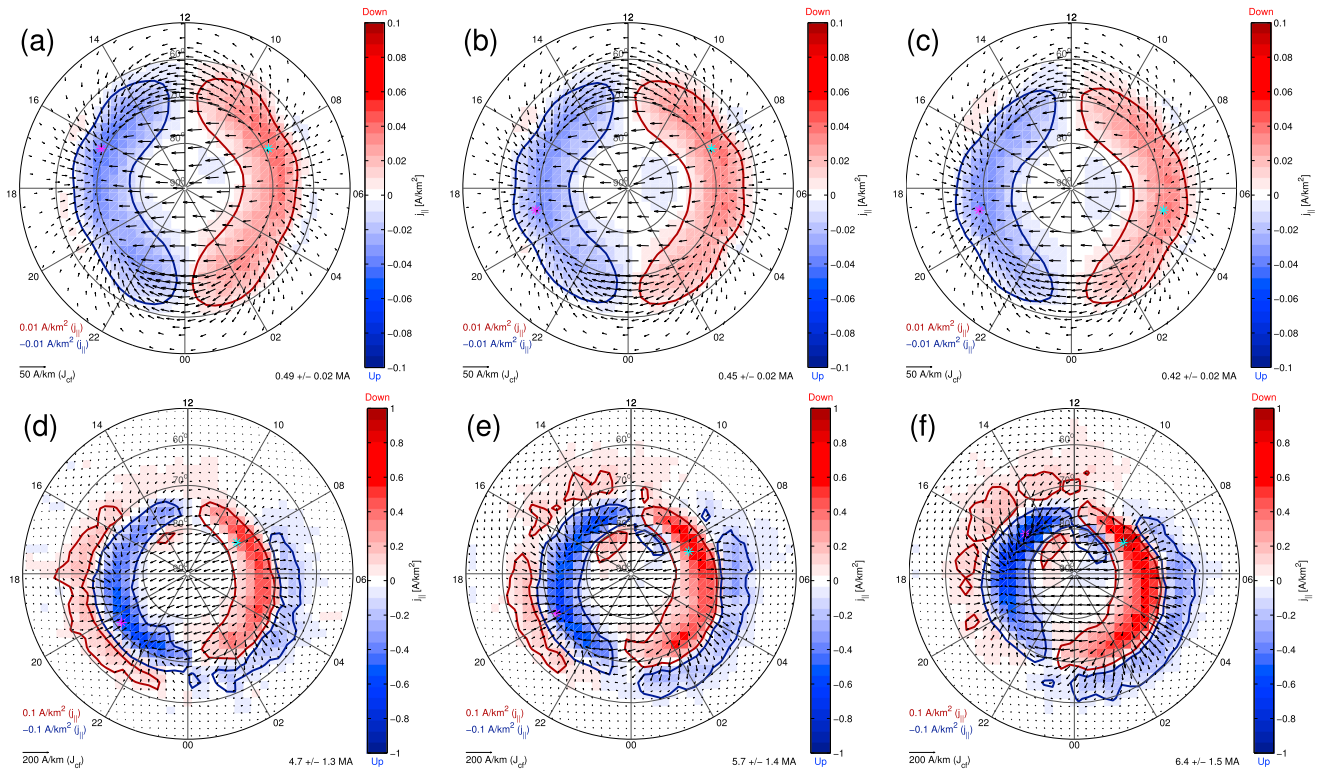
Figure 7. Curl-free component of the horizontal current density (arrows) and field-aligned current density (color) for winter, equinox, and summer (a–c) from GUMICS-4 and (d–f) from CHAMP. The blue and red curves are the ±0.01 A/km^2 in Figures 7a–7c or ±0.1 A/km^2 in Figures 7d–7f contours of the field-aligned current density. The locations of the minimum and maximum field-aligned current density are indicated by the magenta and cyan asterisks, respectively, and the field-aligned current is given in the bottom right corner. Note that the scales for the GUMICS-4 and CHAMP distributions are not identical.

westward electrojet, whereas in GUMICS-4 this current system practically disappears. This is also reflected in the *AL* indices given in the bottom right corner.

Figure 6 shows the uncertainty of the ground B_x for winter, equinox, and summer from GUMICS-4 (a–c) and from CHAMP (d–f). For GUMICS-4, the uncertainty was estimated from the SD of the horizontal ionospheric current density (ΔJ_x and ΔJ_y) using the propagation of error (or uncertainty) [*Taylor*, 1997] and for CHAMP from the SD of the measured magnetic field (ΔB_x, ΔB_y, and ΔB_z). For reference, the blue and red curves indicate the ±10 nT (a–c) or ±20 nT (d–f) contours of the ground B_x from Figure 5. Again, the scales are different for GUMICS-4 and CHAMP. During winter, both GUMICS-4 (Figure 6a) and CHAMP (Figure 6d) show the highest SD under the westward electrojet, although for GUMICS-4 the location is around midnight and for CHAMP in the postmidnight sector. This is very different from the high-latitude noon peak of the SD of the electrostatic potential (Figure 3). While for GUMICS-4 the SD of B_x becomes smaller toward summer, for CHAMP it becomes stronger, particularly on the dayside.

3.3. Field-Aligned Current

Figure 7 shows the curl-free component of the horizontal ionospheric current density (arrows) and the field-aligned current density (color) in the same format as Figure 5, except that the number at the bottom right corner indicates the field-aligned current, calculated as a sum of the absolute value of the field-aligned current density in each grid cell times the area of the grid cell over the grid. The blue and red curves are the ±0.01 A/km^2 (a–c) or ±0.1 A/km^2 (d–f) contours of the field-aligned current density. The main difference in the GUMICS-4 and CHAMP patterns is that where CHAMP shows both the poleward Region 1 and equatorward Region 2 ring of field-aligned current, GUMICS-4 shows mainly the Region 1 field-aligned current with only traces of Region 2 near 60° latitude. Because the Region 2 currents are not present in GUMICS-4, the downward Region 1 current in the dawn sector has to close with the upward Region 1 current in the dusk sector. The two field-aligned current regions of different polarity are linked with horizontal currents across the polar cap. In the CHAMP pattern, the downward Region 1 current in the dawn sector is also linked to the upward Region 1 current in the dusk sector with horizontal current across the polar cap. What is more
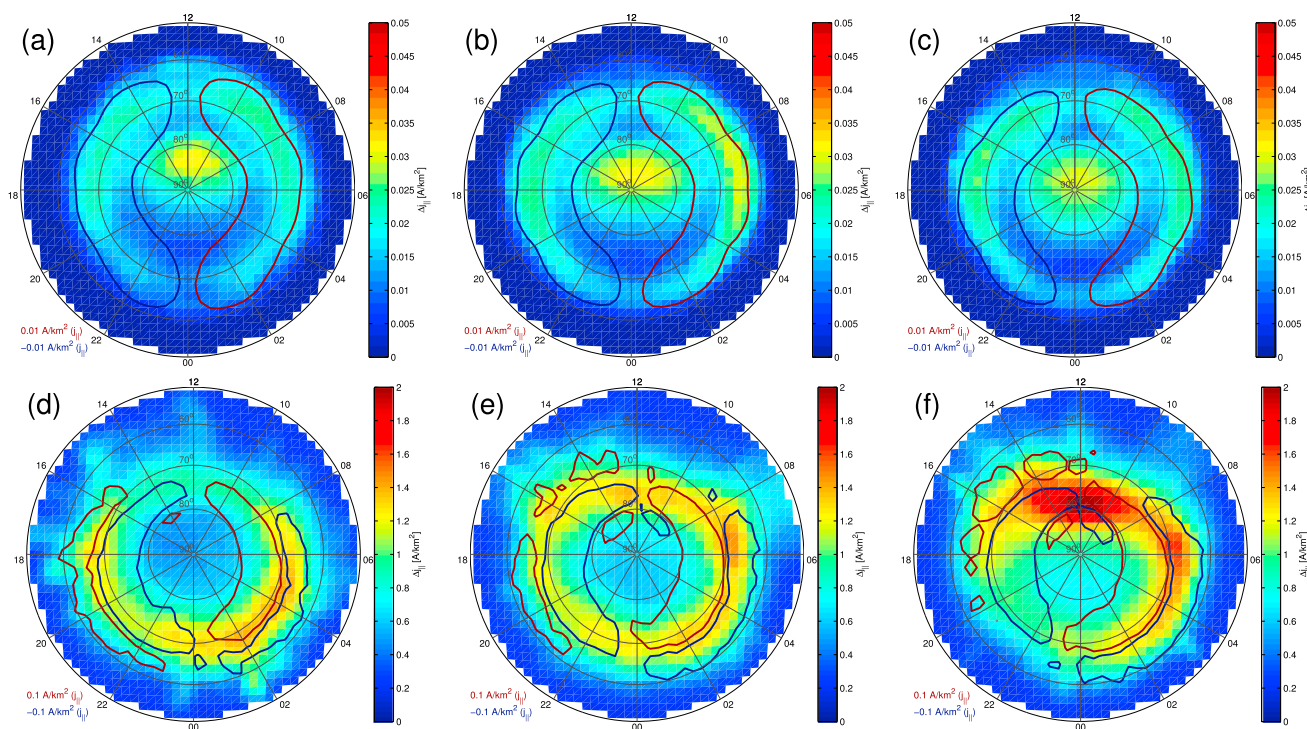
Figure 8. Uncertainty of the field-aligned current density for winter, equinox, and summer (a–c) from GUMICS-4 and (d–f) from CHAMP. For GUMICS-4, the uncertainty is the standard deviation (SD) of the field-aligned current density, and for CHAMP the uncertainty is estimated from the SD of the measured magnetic field (ΔB_x, ΔB_y, and ΔB_z) using the propagation of error. The blue and red curves are the same as in Figure 7. Note that the scales for the GUMICS-4 and CHAMP distributions are not identical.

important, however, is that the downward Region 1 current and the upward Region 2 current in the dawn sector are also linked with horizontal currents across the auroral oval, as are the upward Region 1 current and downward Region 2 current in the dusk sector.

While CHAMP shows a clear enhancement of the total field-aligned current from winter to equinox to summer, particularly on the dayside, for GUMICS-4 the field-aligned current remains practically constant. The maxima of the downward and upward field-aligned current density are related to Region 1 for both CHAMP and GUMICS-4. The maximum downward current density is located on the dayside for all other cases except for GUMICS-4 summer. However, where the maximum upward current density for CHAMP shifts from nightside during winter to dayside during summer, GUMICS-4 shows an opposite behavior. The downward Region 2 current on the duskside derived from CHAMP data forms a region of enhanced ($|j_{||}| > 0.1$ A/km^2) current density on the nightside during winter, one region on the nightside and another on the dayside during equinox, and a region on the dayside during summer. Figure 7 also shows a pair of Region 0 currents poleward of the Region 1 currents, associated with occurrences of northward IMF conditions [e.g., *Juusola et al.*, 2014]. For CHAMP (Figure 7d–7f), the Region 0 currents are located on the dayside and enhance from winter to summer, whereas for GUMICS-4 (Figures 7a–7c), they are more symmetric with respect to the dawn-dusk meridian and remain more or less constant throughout the seasons. The amplitude of the GUMICS-4 Region 0 is weak ($|j_{||}| < 0.01$ A/km^2) compared to Region 1, probably due to the averaging over a long interval with both northward and southward IMF occurrences.

Figures 8a–8c show the SD of the field-aligned current density for winter, equinox, and summer from GUMICS-4. For reference, the blue and red curves indicate the ± 0.01 A/km^2 contours of the mean field-aligned current density from Figures 7a–7c. Figures 8d–8f show the uncertainty of the field-aligned current density from CHAMP, estimated from the SD of the measured magnetic field (ΔB_x, ΔB_y, and ΔB_z) using the propagation of error. The blue and red curves indicate the ± 0.1 A/km^2 contours of the field-aligned current density from Figures 7d–7f. The maximum uncertainty of the field-aligned current density in Figure 8 is larger than the maximum amplitude of the field-aligned current density in Figure 7 for CHAMP (d–f) and comparable in GUMICS-4 (a–c). The uncertainty of the field-aligned current density from CHAMP is largest

between the large-scale structures, i.e., between the Region 1 and Region 2 sheets in the latitudinal direction but also between the duskside and dawnside Region 1 sheets in the MLT direction. This could be related to slightly different locations of the large-scale structures during different IMF conditions as well as to structures that are smaller in size than the 2° grid cells. *Ritter et al.* [2004] have reported that the transition from the downward Region 1 to upward Region 2 on the dawnside occurs above the westward auroral electrojet and is characterized by alternating upward and downward field-aligned currents. Consequently, the most intense upward field-aligned currents were not found in the Region 2 proper but above the auroral electrojet and were suggested to probably give rise to a high conductivity, a requirement for the intense electrojet current. From winter to summer, the highest SD values in Figures 8d–8f shift from the nightside to the dayside, similar to the behavior of the SD of ground B_x in Figures 6d–6f. GUMICS-4 does not show practically any variation in the SD of the field-aligned current density between winter and summer conditions, but similar to the measurements, there are enhanced SD values at the equatorward edge of the Region 1 sheets as well as poleward of about 80° latitude on the dayside, a location which for GUMICS-4 typically lies between the upward and downward Region 0 field-aligned currents [*Janhunen et al.*, 2012]. However, if small-scale structures contribute significantly to the SD values derived from CHAMP data, a good correlation with the SD values derived from GUMICS-4 would not be expected, as such small-scale structures are not present in the GUMICS-4 ionosphere.

4. Discussion

4.1. Precipitation and Conductances

Newell et al. [2009] used DMSP satellite data to investigate the global auroral precipitation budget. They separated the aurora to electron accelerated aurora (both broadband or wave and monoenergetic), ion diffuse aurora, and electron diffuse aurora. According to their results, the dominant contributor (12.6 GW, 61%) to the global precipitation budget averaged over one solar cycle is the diffuse electron aurora. Because of electrons that drift eastward in the inner magnetosphere, the average diffuse aurora energy flux is most intense in the midnight-dawn sector. Diffuse ion aurora (3.4 GW) and accelerated monoenergetic electron aurora (3.3 GW) both contribute 16% to the global budget. Possibly because of ions that drift westward in the inner magnetosphere, the diffuse ion aurora energy flux is most intense in the dusk-midnight sector. Most of the accelerated monoenergetic electron aurora energy flux also precipitates into the dusk-midnight sector, corresponding to the statistical upward Region 1 current. The accelerated wave aurora energy flux peaks in the premidnight sector and contributes 1.5 GW or 6% to the global budget.

There are several aspects in the DMSP picture of precipitation that are different from how precipitation is modeled in GUMICS-4: (1) As only electron precipitation is implemented, there is no diffuse ion aurora contribution. (2) As the ionosphere-magnetosphere potential difference is set to zero (Knight relation [*Knight*, 1973], for example, has not been implemented), there is no dawn-dusk asymmetric accelerated monoenergetic electron aurora contribution. Neither is there accelerated wave aurora contribution. (3) As the MHD description does not include curvature and gradient drifts, there is no corresponding dawn-dusk asymmetry in the diffuse aurora contribution. Thus, the combined energy flux of the different types of aurora precipitation is in GUMICS-4 modeled as rather dawn-dusk symmetrical diffuse electron precipitation, as shown in Figures 9a–9c for winter, equinox, and summer. The blue and red field-aligned current contours from Figures 7a–7c are indicated for reference. The integrated power poleward of 60° latitude is given in the bottom right corner, with the uncertainty estimated from the SD of the precipitation using the propagation of error. These differences in the precipitation between GUMICS-4 and observations indicate that considerable enhancements of the magnetosphere-ionosphere coupling and ionospheric solver are needed before GUMICS-4 or its operational successor code can be used to forecast the geographical distribution of auroral emissions.

Newell et al. [2010] used the DMSP data to examine seasonal variation of the aurora. According to their observations, the global precipitation power for low (high) solar wind driving conditions is 9.8 GW (37.1 GW) in winter, 11.3/11.2 GW (36.5/35.6 GW) in spring/fall, and 9.6 GW (30.8 GW) in summer. The precipitation power in GUMICS-4 is of the same magnitude as the DMSP values for low solar wind driving but shows a clear seasonal trend with values that decrease from winter (14.0 ± 0.6 GW) to equinox (10.8 ± 0.7 GW) to summer (8.8 ± 0.8 GW). According to the observation of *Newell et al.* [2009], the dayside contribution to the global precipitation power for low (high) solar wind driving conditions is 38% (23%) in winter, 36%/38%
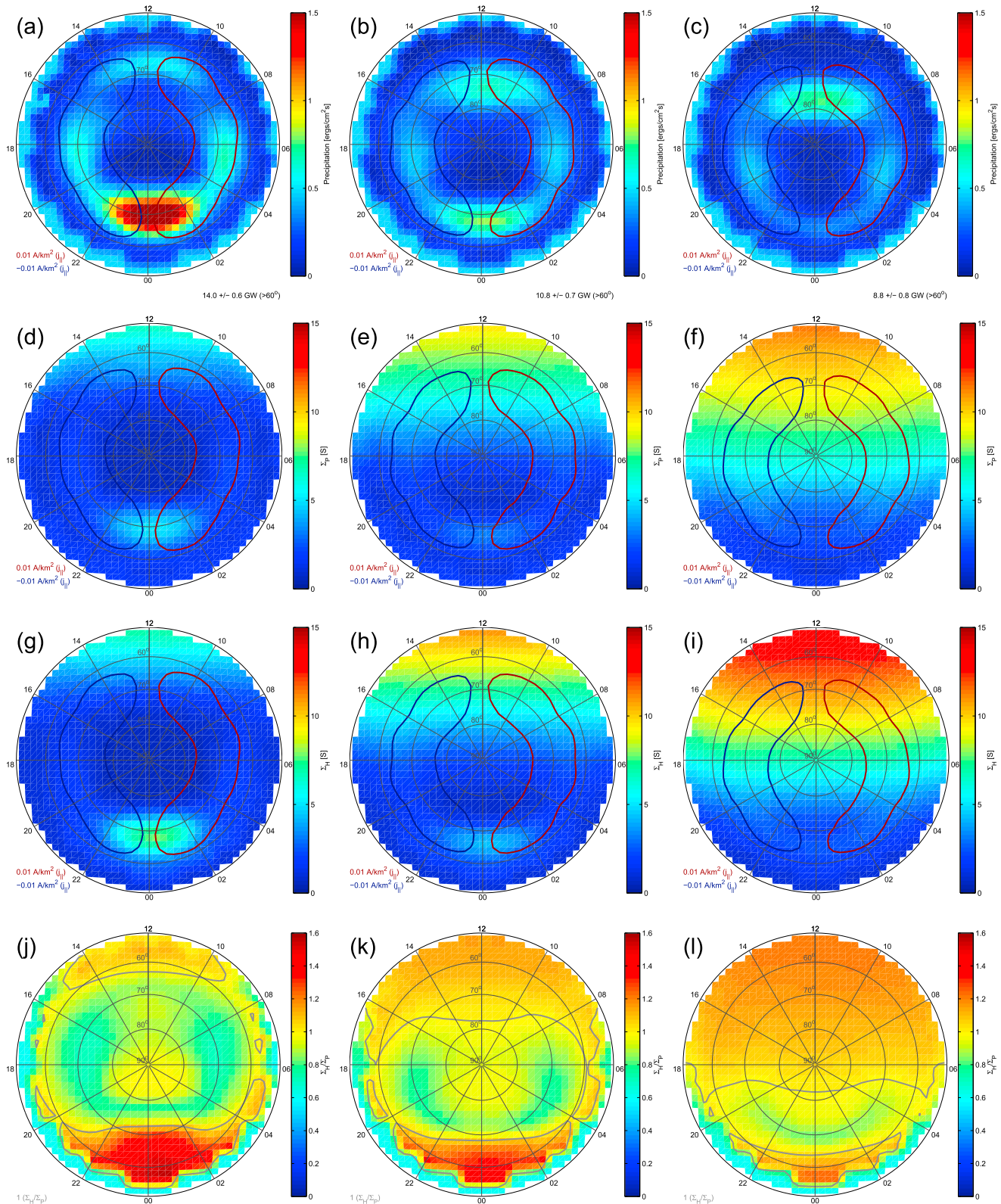
Figure 9. (a–c) Precipitation energy flux for winter, equinox, and summer from GUMICS-4. The blue and red curves are the same as in Figures 7a–7c. The integrated power poleward of 60° latitude is given in the bottom right corner. (d–f) Pedersen conductance Σ_P. (g–i) Hall conductance Σ_H. (j–l) Σ_H/Σ_P. The gray curve is the unity contour of the ratio.

(25%/26%) in spring/fall, and 42% (31%) in summer. The dayside contribution in GUMICS-4 is again of the same order as observations but increases more clearly from winter (36%) to equinox (49%) to summer (55%).

Fuller-Rowell and Evans [1987] showed global statistical patterns of the total electron and ion energy flux incident upon the atmosphere and the height-integrated electron-produced Hall and Pedersen conductivities as a function of auroral activity, constructed from TIROS-NOAA satellite data. Examples for activity levels 3 ("low"), 5 ("average"), 7 ("moderate"), and 9 ("active") were shown, corresponded to estimated particle power inputs to a single hemisphere in the ranges 4–6, 10–16, 24–39, and 61–96 GW, respectively. The precipitation power of GUMICS-4 in Figures 9a–9c falls within the range of the average level 5. *Fuller-Rowell and Evans*'s [1987] energy flux patterns are slightly asymmetric about midnight, peaking about 3 h postmidnight for levels 3 and 5, and 2 h premidnight for levels 7 and 9. The peak intensity increases from around 0.5 ergs cm^{-2} s^{-1} for level 3 to over 6 ergs cm^{-2} s^{-1} for level 9. The peak values for GUMICS-4, 1.8 ergs cm^{-2} s^{-1} for winter and 0.8 ergs cm^{-2} s^{-1} for equinox and summer, are more or less in agreement.

Precipitating electrons produce significant changes in the ionospheric Hall and Pedersen conductivities that in turn have a major effect on the high-latitude electric field and current patterns. Figures 9d–9f show the mean Pedersen conductances and Figures 9g–9i the mean Hall conductances from GUMICS-4 for winter, equinox, and summer, respectively. *Hardy et al.* [1987] used global patterns of the integral energy flux and average energy of precipitating auroral electrons derived from DMSP data to determine the electron-produced Hall and Pedersen conductivities for different levels of activity as measured by the *Kp* index. The resulting conductances varied smoothly with latitude and MLT typically having a single peak in latitude within the auroral oval at any MLT. For the GUMICS-4 winter patterns in Figures 9d and 9g, this is true around midnight but not at other MLTs. The patterns of *Hardy et al.* [1987] are slightly asymmetric about midnight with the lowest peak values found postnoon. *Fuller-Rowell and Evans*'s [1987] patterns are similarly asymmetric, with the peak moving from postmidnight to premidnight as the level of activity increases. GUMICS-4 patterns, on the other hand, are more or less symmetric. According to *Hardy et al.* [1987], the peak value of the Pedersen (Hall) conductance varies from 3 (4) mhos to 13 (26) mhos as *Kp* varies from 0 to ≥ 6, and according to *Fuller-Rowell and Evans* [1987], it is 4 (4), 7 (8), 10 (13), and 16 (23) mho for the activity levels 3, 5, 7, and 9, respectively. The peak nightside winter (the smallest solar contribution) Pedersen (Hall) conductance value for GUMICS-4 in Figure 9d (Figure 9g) is 5 (8) S (= mho), in agreement with the observations for average activity level.

Ridley [2007] discussed the effects of the seasonal changes in the ionospheric conductances on field-aligned currents when the potential does not change significantly. *Ridley* [2007] demonstrated that if only solar radiation-driven variations in the conductances are considered, the ratio between the maximum winter and maximum summer field-aligned current density would be about 4. However, when a seasonally varying auroral precipitation model (*Fuller-Rowell and Evans* [1987] driven using a seasonally varying hemispheric power with a value of about 6 GW for winter solstice and about 1 GW for summer solstice) is used to increase the conductance in winter, the ratio is reduced to 1.6, which is in agreement with observations [e.g., *Fujii et al.*, 1981; *Papitashvili et al.*, 2002; *Christiansen et al.*, 2002]. The amplitudes of the maximum downward (upward) field-aligned current from CHAMP in our Figures 7d–7f are 0.54 (−0.59) A/km^2 for winter, 0.67 (−0.66) A/km^2 for equinox, and 0.91 (−0.81) A/km^2 for summer, respectively. Unlike the upward current maximum, the downward current maximum remains on the dayside, and the ratio between the winter and summer values is 0.91/0.54 = 1.7, in agreement with earlier observations and *Ridley* [2007]. Although in GUMICS-4 the ratio between the winter and summer downward current maxima is more or less constant, the winter conductances are enhanced on the nightside and the summer conductances on the dayside, which is in line with the conclusion of *Ridley* [2007]. However, compared to the model conductances of *Ridley* [2007], the nightside enhancement in GUMICS-4 is confined around midnight, instead of extending throughout the auroral oval, and particularly on the dawnside.

Figures 9j–9l show the mean ratio of the Hall and Pedersen conductances, which provides information on the characteristic energy of the particle spectrum producing the enhanced ionization on the nightside [e.g., *Robinson et al.*, 1987]. The gray curves indicate the unity contours of the ratio. Of course, in the regions where the conductivities include a solar contribution, the ratio will not represent a true indicator of the hardness of precipitating electrons. According to *Fuller-Rowell and Evans* [1987], the ratio is generally in the range 1.0–1.6, and according to *Hardy et al.* [1987] and *Juusola et al.* [2007], the highest values of the ratio are found on the dawnside of the oval. Again, the GUMICS-4 winter pattern in Figure 9f does not show the

observed dawn-dusk asymmetry, and the values of the ratio fall between 1.0 and 1.6 only in a relatively small region around midnight. In particular, the values in the dawn and dusk sectors are < 1 and do not show the auroral oval.

Thus, although the numerical values of the peak precipitation energy, Hall conductance, Pedersen conductance, and the conductance ratio appear to be in good agreement with observations, their distributions are not. Unlike observations, the GUMICS-4 distributions are dawn-dusk symmetric and do not produce a band of increased values around the pole, i.e., the auroral oval. The dawn-dusk symmetry is a consequence of the MHD description and is therefore not easily removed in future developments of the model. This sets a limitation on the usability of MHD codes for geographically localized space weather forecasts. The good agreement of the peak values with observations suggests that for forecast purposes one might use a globally descriptive peak or integrated value from the simulation in conjunction with an empirical model that would give the form of the spatial distribution.

The precipitation power is also in good agreement with observations, but the seasonal trend of weakening nightside precipitation and strengthening dayside precipitation from winter to summer may be too drastic. Especially in the summer, the contrast between the precipitation and UV contributions to the GUMICS-4 conductances appears to be too small.

Field-aligned current and precipitation are not necessarily compatible in GUMICS-4, such that precipitating electrons would carry upward field-aligned current. This can be seen in Figures 9a–9c, for example, where regions of upward and downward field-aligned current are indicated by the blue and red contours, respectively. The most intense precipitation occurs between the regions of upward and downward current, not in the region of upward current. Whether this may or may not be a problem is not clear, however. The large-scale Region 1 and Region 2 field-aligned current systems derived from CHAMP measurements are statistical concepts, and the compatibility of currents and precipitation may occur at the level of the embedded smaller-scale current structures [e.g., *Ritter et al.*, 2004] rather than at the level of the large-scale ones.

4.2. Voltage Generator or Current Generator

Our SuperDARN observation that the ionospheric cross polar cap potential drop does not change significantly throughout the seasons is in agreement with the result of *Weimer* [1995]. According to *de la Beaujardiere et al.* [1991], the cross polar cap potential drop varies as a function of season, being the largest in fall, followed by winter, spring, and summer. However, the difference between spring and fall and between summer and winter were of the order of 8 and 5 kV, which represents only 5–10% of the total potential drop across the polar cap. The small difference between the summer and winter cross polar cap potential was suggested to be attributable to differing field-aligned potential drop. *Rich and Hairston* [1994] also found a small but statistically significant difference in the cross polar cap potential drop between seasons.

The two most significant contributors to the ionospheric conductances are solar radiation, which changes drastically throughout the seasons of the year, and auroral precipitation. According to our observations, the electrostatic potential remains practically constant throughout the seasons while variations in the conductances are mainly accommodated through variations in the horizontal ionospheric currents, in accordance with Ohm's law, and the field-aligned currents that close them. This indicates that the solar wind and magnetosphere behave like a voltage generator, at least on the dayside [e.g., *Fujii et al.*, 1981; *Wang et al.*, 2005]. According to *Wing et al.* [2010, 2011], the dayside Region 1 is frequently observed to be located on open magnetospheric field lines or at the low-latitude boundary layer, where the dominant current generation mechanism is velocity shear across the magnetopause. Thus, a voltage-driven current would be expected. In GUMICS-4 the behavior is opposite: the field-aligned currents remain constant throughout the season while the electrostatic potential varies. Thus, the GUMICS-4 MHD domain behaves like a current generator, both on the dayside and on the nightside. In GUMICS-4, the magnetosphere-ionosphere coupling is implemented so that at each simulation step field-aligned current is calculated from $(\nabla \times \mathbf{B}) \cdot \mathbf{B}_{dipole}$ at the inner boundary of the MHD domain and is mapped down to the ionosphere along dipole field lines. The ionospheric potential solver takes the field-aligned current and separately calculated conductances as the input and gives the corresponding perpendicular electrostatic potential as output. This potential is mapped back to the inner boundary of the MHD domain, where it is used as a new boundary condition for the MHD solver. In principle, this magnetosphere-ionosphere coupling scheme should work equally well regardless of the MHD domain's behavior (e.g., current or voltage generator), as the equilibrium between the MHD and ionospheric domains

is ultimately based on current continuity and mapping of the electric field along the field lines. However, a different implementation of the coupling process [e.g., *Janhunen*, 1998; *Yoshikawa et al.*, 2011] should be tested in future development of GUMICS-5 to decisively check whether the magnetosphere-ionosphere coupling scheme can change large-scale behavior of the MHD magnetosphere.

Assuming that the potential on the open polar cap field lines is directly determined by the solar wind, it would be expected to be more or less the same in the winter and summer hemispheres. However, because the Region 2 field-aligned current system is missing in GUMICS-4, the Region 1 field-aligned current has to close across the polar caps instead of the auroral ovals. In winter, conductances in the polar cap are small, and a high CPCP is required to drive the current. In summer, the conductances in the polar cap are higher, and only a small CPCP is needed to drive a current of the same amplitude. This probably explains the seasonal behavior of the GUMICS-4 CPCP. Our result agrees with those of *Gordeev et al.* [2013], who observed a systematically lower (~10–15%) GUMICS-4 polar cap potential for $F_{10.7}$ solar radio flux conditions corresponding to the higher values at "solar maximum" than the lower values at "solar minimum." No effect on the magnetopause or magnetotail configuration was observed.

Equatorward of the open field line polar caps lies the region of closed magnetic field lines. If the magnetosphere-ionosphere potential difference is zero, and the potential difference along a field line within the MHD domain is assumed to be zero, a field line from one ionospheric hemisphere should map to a region of the same potential in the other ionospheric hemisphere. As long as the maximum and minimum of the potential are the same in both ionospheric hemispheres, magnetic flux tubes within the MHD domain can twist such that regions of equal ionospheric potential are connected. The twisting will then produce tension on the field lines. However, if the potential difference is much higher in one ionospheric hemisphere, no region of equal potential can be found anywhere in the opposite ionospheric hemisphere. The question then is where would those field lines map? It is unlikely that field-aligned potential drops within the MHD domain could explain the large hemispherical potential differences observed in GUMICS-4 ionosphere. Of course, the electrostatic potential Φ does not appear directly in the MHD equations. The electric field is calculated as $\mathbf{E} = -\mathbf{V} \times \mathbf{B}$, with often $\nabla \times \mathbf{E} = -\partial \mathbf{B}/\partial t \neq 0$. Thus, checking how the potential satisfying $\mathbf{E} = -\nabla \Phi$ varies along a magnetic field line within the MHD domain may not be straightforward or even meaningful.

4.3. Inner Magnetosphere

As an MHD-based model, GUMICS-4 has some limitations. In particular, the plasma in the inner magnetosphere, which consists of overlapping hot ring current and cold plasmaspheric populations, cannot accurately be described using a single MHD fluid with a single temperature [e.g., *Janhunen et al.*, 2012]. Using MHD to approximate the multicomponent character of the plasma can be one reason the plasma pressure in the inner magnetosphere produced by GUMICS-4 is weak compared to observations. Possible other reasons include too coarse grid resolution and/or too large inner boundary distance (3.7 R_E). Decreasing the inner boundary radius would seem a straightforward amelioration but is computationally very expensive, because close to Earth the Alfvén speed rises rapidly and the largest possible time step decreases respectively. The weak pressure gradients lead to weak field-aligned current density in the ionosphere, especially the Region 2 system at the equatorward boundary of the auroral ovals. Furthermore, the curvature and gradient drifts missing from the MHD description may play a role in the distribution of the ionospheric particle precipitation and the resulting conductances. This could be one reason there is no proper auroral oval in GUMICS-4. Even if the Region 2 current system could be enhanced in GUMICS, the lack of the highly conducting band may still distort the current closure.

Because of the weak pressure in the inner magnetosphere, magnetospheric processes, such as plasma flows, could penetrate closer to Earth than what is observed. This could be one reason the signatures of electrodynamic coupling between magnetosphere and ionosphere extend to lower latitudes in GUMICS-4 than in observations.

4.4. Other Global MHD Models

The results presented here may, to some extent, also be applicable to the other global MHD models available through the Community Coordinated Modeling Center (CCMC): Block-Adaptive Tree Solar wind Roe-type Upwind Scheme (BATS-R-US), Lyon-Fedder-Mobarry (LFM), and Open General Geospace Circulation Model (OpenGGCM). All these models couple the magnetosphere and ionosphere through field-aligned currents and electric potential mapped along a dipole field. Ohm's law, combined with current continuity and the electrostatic approximation, is used to calculate the perpendicular ionospheric electric potential,

given the field-aligned current at the top of the ionospheric conducting layer and the height-integrated conductances. However, there are also differences between the simulations [*Honkonen et al.*, 2013, and references therein].

Honkonen et al. [2013] compared the performance of the BATS-R-US, GUMICS-4, LFM, and OpenGGCM models available at CCMC. During an event on 18 February 2004 between 15 and 24 UT, BATS-R-US produced the best agreement with SuperDARN CPCP. GUMICS-4 and LFM were able to capture the dynamics of CPCP, but the results differed from SuperDARN by a constant factor of about 0.7 and 3, respectively. OpenGGCM was also able to reproduce the general behavior of CPCP, but with occasional discrepancies.

Zhang et al. [2011] examined statistically the magnetosphere-ionosphere coupling in a 2 month long spring equinox LFM run. The inner computational boundary was set at 2.2 R_E, which is closer to Earth than in GUMICS-4. The average field-aligned current distribution and amplitude produced by LFM, including both Region 1 and Region 2 systems, were found to be similar to those observed by the Iridium satellite constellation. The Region 2 currents in LFM mainly originate from the divergence of an MHD diamagnetic current. The ionospheric convection patterns were also found to be in reasonable agreement with SuperDARN measurements, although the simulated patterns were more dawn-dusk symmetric than observations. However, the average CPCP was a factor of 2 higher than that measured by SuperDARN. Similar to GUMICS-4, most of the dawnside Region 1 current in LFM was found to close to the duskside Region 1 current through the polar region, as opposed to observations in which Region 1 current closes with Region 2 current. This feature of the simulation was attributed to the high CPCP.

Merkin et al. [2013] compared ionospheric field-aligned current patterns from a high-resolution (sub-100 km in the ionosphere) LFM simulation with the Active Magnetosphere and Planetary Electrodynamics Response Experiment (AMPERE) field-aligned currents derived from Iridium data for a ∼40 min event on 3 August 2010. They concluded that given sufficient resolution, contemporary global MHD models are capable of reproducing observed features of global field-aligned current distributions. Unfortunately, repeating the GUMICS-4 1 year run with a higher resolution (e.g., adaptation level 6) would not be feasible at the moment because of the increase in computational time.

Korth et al. [2011] showed that a simulation code that includes an inner magnetosphere module (Rice Convection Model) in addition to a global MHD magnetosphere module (BATS-R-US, inner computational boundary at 3 R_E) and an ionosphere module is also able to reproduce the spatial distributions of Iridium statistical field-aligned currents. The model was run for equinox conditions.

5. Conclusions

In this study, we have carried out a statistical comparison of the seasonal variations of simulated and observed ionospheric parameters. The simulated data comprised a set of GUMICS-4 runs that were fed with real solar wind data and covered the period from 30 January 2002 to 2 February 2003. The GUMICS-4 model consists of an MHD solar wind and magnetosphere and an electrostatic ionosphere. Distributions of the perpendicular ionospheric electrostatic potential and convection were derived from SuperDARN radar measurements and distributions of the horizontal and field-aligned ionospheric current density from the magnetic field measured by the CHAMP satellite. Time series of the cross polar cap potential were also obtained from SuperDARN, and the *AL* and *AU* indices were used to examine the behavior of the disturbance magnetic field on ground. Our main conclusions are the following:

1. The signatures of electrodynamic coupling between the magnetosphere and ionosphere extend to lower latitudes in the GUMICS-4 simulation than in observations, and key features of the auroral ovals, the Region 2 field-aligned currents, electrojets, Harang discontinuity, and enhanced conductivity are not properly reproduced. The weak electrojets produce a ground magnetic field that, even at best, is about 5 times weaker than observations.
2. According to SuperDARN measurements, the perpendicular ionospheric electrostatic potential does not change significantly from winter to summer but field-aligned currents derived from CHAMP measurements enhance. In GUMICS-4, on the other hand, the perpendicular electrostatic potential weakens from winter to summer but field-aligned currents do not change. This could be a consequence of the ionospheric current closure in GUMICS-4: because of the missing Region 2 currents and the relatively low conductivity in the auroral oval, the Region 1 current has to close mainly with itself across the polar

cap, which makes it sensitive to solar UV-induced conductivity variations. According to observations, a significant portion of Region 1 current closes with Region 2 across the highly conducting auroral oval.

3. In GUMICS-4, the peak precipitation energy, Hall conductance, Pedersen conductance, and the ratio of the two conductances are in agreement with observations, but, unlike observations, the GUMICS-4 distributions are dawn-dusk symmetric and do not form a highly conducting band around magnetic pole, i.e., the auroral oval.

When future versions of GUMICS or global MHD simulations, in general, are used to forecast space weather, geographical distributions of ionospheric quantities must be interpreted very cautiously. Globally descriptive ionospheric quantities, such as peak values or spatial integrals, may be more reliable. Even they may need empirical scaling to correct, e.g., differences in seasonal variation with observations.

References

Amm, O. (1997), Ionospheric elementary current systems in spherical coordinates and their application, *J. Geomagn. Geoelec.*, *49*, 947–955.

Amm, O., and A. Viljanen (1999), Ionospheric disturbance magnetic field continuation from the ground to ionosphere using spherical elementary current systems, *Earth Planets Space*, *51*, 431–440.

Baker, K. B., and S. Wing (1989), A new magnetic coordinate system for conjugate studies at high latitudes, *J. Geophys. Res.*, *94*(A7), 9139–9143, doi:10.1029/JA094iA07p09139.

Boteler, D. H., R. J. Pirjola, and H. Nevanlinna (1998), The effects of geomagnetic disturbances on electrical systems at the Earth's surface, *Adv. Space Res.*, *22*, 17–27, doi:10.1016/S0273-1177(97)01096-X.

Caan, M. N., R. L. McPherron, and C. T. Russell (1978), The statistical magnetic signature of magnetospheric substorms, *Planet. Space Sci.*, *26*(3), 269–279, doi:10.1016/0032-0633(78)90092-2.

Chisham, G., et al. (2007), A decade of the Super Dual Auroral Radar Network (SuperDARN): Scientific achievements, new techniques and future directions, *Surv. Geophys.*, *28*, 33–109, doi:10.1007/s10712-007-9017-8.

Christiansen, F., V. O. Papitashvili, and T. Neubert (2002), Seasonal variations of high-latitude field-aligned currents inferred from ørsted and Magsat observations, *J. Geophys. Res.*, *107*(A2), 1029, doi:10.1029/2001JA900104.

Davis, T. N., and M. Sugiura (1966), Auroral electrojet activity index AE and its universal time variations, *J. Geophys. Res.*, *71*, 785–801.

de la Beaujardiere, O., D. Alcayde, J. Fontanari, and C. Leger (1991), Seasonal dependence of high-latitude electric fields, *J. Geophys. Res.*, *96*(A4), 5723–5735, doi:10.1029/90JA01987.

Fujii, R., T. Iijima, T. A. Potemra, and M. Sugiura (1981), Seasonal dependence of large-scale Birkeland currents, *Geophys. Res. Lett.*, *8*(10), 1103–1106.

Fukushima, N. (1976), Generalized theorem for no ground magnetic effect of vertical currents connected with Pedersen currents in the uniform-conductivity ionosphere, *Rep. Ionos. Space Res. Jpn.*, *30*, 35–40.

Fuller-Rowell, T. J., and D. S. Evans (1987), Height-integrated Pedersen and Hall conductivity patterns inferred from the TIROS-NOAA satellite data, *J. Geophys. Res.*, *92*(A7), 7606–7618, doi:10.1029/JA092iA07p07606.

Gonzalez, W. D., and F. S. Mozer (1974), A quantitative model for the potential resulting from reconnection with an arbitrary interplanetary magnetic field, *J. Geophys. Res.*, *79*(28), 4186–4194, doi:10.1029/JA079i028p04186.

Gordeev, E., G. Facskó, V. Sergeev, I. Honkonen, M. Palmroth, P. Janhunen, and S. Milan (2013), Verification of the GUMICS-4 global MHD code using empirical relationships, *J. Geophys. Res. Space Physics*, *118*, 3138–3146, doi:10.1002/jgra.50359.

Greenwald, R. A., et al. (1995), DARN/SuperDARN: A global view of the dynamics of high-latitude convection, *Space Sci. Rev.*, *71*(1–4), 761–796.

Hardy, D. A., M. S. Gussenhoven, R. Raistrick, and W. J. McNeil (1987), Statistical and functional representations of the pattern of auroral energy flux, number flux, and conductivity, *J. Geophys. Res.*, *92*(A11), 12,275–12,294, doi:10.1029/JA092iA11p12275.

Hedin, A. E. (1991), Extension of the MSIS thermosphere model into the middle and lower atmosphere, *J. Geophys. Res.*, *96*, 1159–1172.

Honkonen, I., L. Rastätter, A. Grocott, A. Pulkkinen, M. Palmroth, J. Raeder, A. J. Ridley, and M. Wiltberger (2013), On the performance of global magnetohydrodynamic models in the Earth's magnetosphere, *Space Weather*, *11*, 313–326, doi:10.1002/swe.20055.

Imber, S. M., S. E. Milan, and M. Lester (2013), Solar cycle variations in polar cap area measured by the SuperDARN radars, *J. Geophys. Res. Space Physics*, *118*, 6188–6196, doi:10.1002/jgra.50509.

Janhunen, P. (1998), On the possibility of using an electromagnetic ionosphere in global MHD simulations, *Ann. Geophys.*, *16*, 397–402, doi:10.1007/s00585-998-0397-y.

Janhunen, P., M. Palmroth, T. Laitinen, I. Honkonen, L. Juusola, G. Facskó, and T. I. Pulkkinen (2012), The GUMICS-4 global MHD magnetosphere-ionosphere coupling simulation, *J. Atmos. Sol. Terr. Phys.*, *80*, 48–59, doi:10.1016/j.jastp.2012.03.006.

Juusola, L., O. Amm, K. Kauristie, and A. Viljanen (2007), A model for estimating the relation between the Hall to Pedersen conductance ratio and ground magnetic data derived from CHAMP satellite statistics, *Ann. Geophys.*, *25*(3), 721–736.

Juusola, L., S. E. Milan, M. Lester, A. Grocott, and S. Imber (2014), Interplanetary magnetic field control of the ionospheric field-aligned current and convection distributions, *J. Geophys. Res. Space Physics*, *119*, 3130–3149, doi:10.1002/2013JA019455.

Kempf, Y., D. Pokhotelov, S. von Alfthan, A. Vaivads, M. Palmroth, and H. E. J. Koskinen (2013), Wave dispersion in the hybrid-Vlasov model: Verification of Vlasiator, *Phys. Plasmas*, *20*, 112114, doi:10.1063/1.4835315.

Knight, S. (1973), Parallel electric fields, *Planet. Space Sci.*, *21*(5), 741–750, doi:10.1016/0032-0633(73)90093-7.

Korth, H., L. Rastätter, B. J. Anderson, and A. J. Ridley (2011), Comparison of the observed dependence of large-scale Birkeland currents on solar wind parameters with that obtained from global simulations, *Ann. Geophys.*, *29*(10), 1809–1826, doi:10.5194/angeo-29-1809-2011.

Koskinen, H. E. J., and T. I. Pulkkinen (1995), Midnight velocity shear zone and the concept of Harang discontinuity, *J. Geophys. Res.*, *100*(A6), 9539–9547, doi:10.1029/95JA00228.

Laitinen, T. V., T. I. Pulkkinen, M. Palmroth, P. Janhunen, and H. E. J. Koskinen (2005), The magnetotail reconnection region in a global MHD simulation, *Ann. Geophys.*, *23*, 3753–3764, doi:10.5194/angeo-23-3753-2005.

Laitinen, T. V., M. Palmroth, T. I. Pulkkinen, P. Janhunen, and H. E. J. Koskinen (2007), Continuous reconnection line and pressure-dependent energy conversion on the magnetopause in a global MHD model, *J. Geophys. Res.*, *112*, A11201, doi:10.1029/2007JA012352.

Maus, S., M. Rother, C. Stolle, W. Mai, S. Choi, H. Lühr, D. Cooke, and C. Roth (2006), Third generation of the Potsdam Magnetic Model of the Earth (POMME), *Geochem. Geophys. Geosyst.*, *7*, Q07008, doi:10.1029/2006GC001269.

Merkin, V. G., B. J. Anderson, J. G. Lyon, H. Korth, M. Wiltberger, and T. Motoba (2013), Global evolution of Birkeland currents on 10 min timescales: MHD simulations and observations, *J. Geophys. Res. Space Physics*, *118*, 4977–4997, doi:10.1002/jgra.50466.

Milan, S. E., T. A. Evans, and B. Hubert (2010), Average auroral configuration parameterized by geomagnetic activity and solar wind conditions, *Ann. Geophys.*, *28*(4), 1003–1012, doi:10.5194/angeo-28-1003-2010.

Moen, J., and A. Brekke (1993), The solar flux influence on quiet time conductances in the auroral ionosphere, *Geophys. Res. Lett.*, *20*, 971–974.

Newell, P. T., T. Sotirelis, and S. Wing (2009), Diffuse, monoenergetic, and broadband aurora: The global precipitation budget, *J. Geophys. Res.*, *114*, A09207, doi:10.1029/2009JA014326.

Newell, P. T., T. Sotirelis, and S. Wing (2010), Seasonal variations in diffuse, monoenergetic, and broadband aurora, *J. Geophys. Res.*, *115*, A03216, doi:10.1029/2009JA014805.

Palmroth, M., I. Honkonen, A. Sandroos, Y. Kempf, S. von Alfthan, and D. Pokhotelov (2013), Preliminary testing of global hybrid-Vlasov simulation: Magnetosheath and cusps under northward interplanetary magnetic field, *J. Atmos. Sol. Terr. Phys.*, *99*, 41–46, doi:10.1016/j.jastp.2012.09.013.

Papitashvili, V. O., F. Christiansen, and T. Neubert (2002), A new model of field-aligned currents derived from high-precision satellite magnetic field data, *Geophys. Res. Lett.*, *29*(14), 1683, doi:10.1029/2001GL014207.

Pokhotelov, D., S. von Alfthan, Y. Kempf, R. Vainio, H. E. J. Koskinen, and M. Palmroth (2013), Ion distributions upstream and downstream of the Earth's bow shock: First results from Vlasiator, *Ann. Geophys.*, *31*, 2207–2212, doi:10.5194/angeo-31-2207-2013.

Pulkkinen, A., et al. (2013), Community-wide validation of geospace model ground magnetic field perturbation predictions to support model transition to operations, *Space Weather*, *11*, 369–385, doi:10.1002/swe.20056.

Rich, F. J., and M. Hairston (1994), Large-scale convection patterns observed by DMSP, *J. Geophys. Res.*, *99*(A3), 3827–3844, doi:10.1029/93JA03296.

Ridley, A. J. (2007), Effects of seasonal changes in the ionospheric conductances on magnetospheric field-aligned currents, *Geophys. Res. Lett.*, *34*, L05101, doi:10.1029/2006GL028444.

Ritter, P., H. Lühr, A. Viljanen, O. Amm, A. Pulkkinen, and I. Sillanpää (2004), Ionospheric currents estimated simultaneously from CHAMP satellite and IMAGE ground-based magnetic field measurements: A statistical study at auroral latitudes, *Ann. Geophys.*, *22*(2), 417–430.

Robinson, R. M., R. R. Vondrak, K. Miller, T. Dabbs, and D. Hardy (1987), On calculating ionospheric conductances from the flux and energy of precipitating electrons, *J. Geophys. Res.*, *92*(A3), 2565–2569.

Roe, P. L. (1981), Approximate Riemann solvers, parameter vectors, and difference schemes, *J. Comput. Phys.*, *43*(2), 357–372, doi:10.1016/0021-9991(81)90128-5.

Ruohoniemi, J. M., and K. B. Baker (1998), Large-scale imaging of high-latitude convection with Super Dual Auroral Radar Network HF radar observations, *J. Geophys. Res.*, *103*(A9), 20,797–20,811, doi:10.1029/98JA01288.

Russell, C. T., and R. L. McPherron (1973), Semiannual variation of geomagnetic activity, *J. Geophys. Res.*, *78*(1), 92–108.

Sandroos, A., I. Honkonen, S. von Alfthan, and M. Palmroth (2013), Multi-GPU simulations of Vlasov's equation using Vlasiator, *Parallel Comput.*, *39*(8), 306–318, doi:10.1016/j.parco.2013.05.001.

Sonnerup, B. U. Ö. (1974), Magnetopause reconnection rate, *J. Geophys. Res.*, *79*, 1546–1549.

Taylor, J. R. (1997), *An Introduction to Error Analysis: The Study of Uncertainties in Physical Measurements*, 75 pp., 2nd ed., Univ. Science Books, Sausalito, Calif.

Untiedt, J., and W. Baumjohann (1993), Studies of polar current systems using the IMS Scandinavian magnetometer array, *Space Sci. Rev.*, *63*, 245–390.

Wang, H., H. Lühr, and S. Y. Ma (2005), Solar zenith angle and merging electric field control of field-aligned currents: A statistical study of the southern hemisphere, *J. Geophys. Res.*, *110*, A03306, doi:10.1029/2004JA010530.

Weimer, D. R. (1995), Models of high-latitude electric potentials derived with a least error fit of spherical harmonic coefficients, *J. Geophys. Res.*, *100*(A10), 19,595–19,607, doi:10.1029/95JA01755.

Wing, S., S. Ohtani, P. T. Newell, T. Higuchi, G. Ueno, and J. M. Weygand (2010), Dayside field-aligned current source regions, *J. Geophys. Res.*, *115*, A12215, doi:10.1029/2010JA015837.

Wing, S., S. Ohtani, J. R. Johnson, M. Echim, P. T. Newell, T. Higuchi, G. Ueno, and G. R. Wilson (2011), Solar wind driving of dayside field-aligned currents, *J. Geophys. Res.*, *116*, A08208, doi:10.1029/2011JA016579.

Yoshikawa, A., O. Amm, H. Vanhamäki, and R. Fujii (2011), A self-consistent synthesis description of magnetosphere-ionosphere coupling and scale-dependent auroral process using shear Alfvén wave, *J. Geophys. Res.*, *116*, A08218, doi:10.1029/2011JA016460.

Zhang, B., W. Lotko, M. J. Wiltberger, O. J. Brambles, and P. A. Damiano (2011), A statistical study of magnetosphere ionosphere coupling in the Lyon-Fedder-Mobarry global MHD model, *J. Atmos. Sol. Terr. Phys.*, *73*(5–6), 686–702, doi:10.1016/j.jastp.2010.09.027.